

# Optimizing strong light-matter coupling of plasmonic lattices and monolayer semiconductors

Lukas Krelle,<sup>1,2</sup> Lukas Husel,<sup>1,3</sup> Kenji Watanabe,<sup>4</sup> Takashi Taniguchi,<sup>5</sup>  
Ismail Bilgin,<sup>1,6</sup> Alexander Högele,<sup>1,7,\*</sup> and Farsane Tabataba-Vakili<sup>1,7,8,9,†</sup>

<sup>1</sup>*Fakultät für Physik, Munich Quantum Center, and Center for NanoScience (CeNS),  
Ludwig-Maximilians-Universität München, Geschwister-Scholl-Platz 1, 80539 München, Germany*

<sup>2</sup>*Institute for Condensed Matter Physics, Technische Universität Darmstadt, Hochschulstraße 6, 64289 Darmstadt, Germany*

<sup>3</sup>*Department of Physics, University of Basel, 4056 Basel, Switzerland*

<sup>4</sup>*Research Center for Electronic and Optical Materials,  
National Institute for Materials Science, 1-1 Namiki, Tsukuba 305-0044, Japan*

<sup>5</sup>*Research Center for Materials Nanoarchitectonics,  
National Institute for Materials Science, 1-1 Namiki, Tsukuba 305-0044, Japan*

<sup>6</sup>*Faculty of Engineering, Department of Metallurgical and Materials Engineering,  
Karadeniz Technical University, Trabzon 61080, Türkiye*

<sup>7</sup>*Munich Center for Quantum Science and Technology (MCQST), Schellingstraße 4, 80799 München, Germany*

<sup>8</sup>*Institute of Condensed Matter Physics, Technische Universität Braunschweig, 38106 Braunschweig, Germany*

<sup>9</sup>*Laboratory for Emerging Nanometrology Braunschweig, 38106 Braunschweig, Germany*

(Dated: May 15, 2026)

Exciton-polaritons provide a versatile platform for the study of a wide range of phenomena, including polariton lasers, topological polaritons, and bosonic condensation. Transition metal dichalcogenide monolayers host excitons with large oscillator strength and binding energies constituting a robust matter constituent that forms polaritons from cryogenic to room temperature when embedded in optical microcavities. Plasmonic nanoparticles arranged in lattice geometries offer strong field-confinement and high quality factors. However, the high sensitivity of monolayer excitons to strain and dielectric disorder necessitates encapsulation in atomically flat hBN to ensure a high optical quality, rendering plasmonics more challenging. Here, we employ our recently developed fabrication method for embedding gold nanodisk arrays into van der Waals heterostructures and compare two samples with opposite layer order. We observe that strain and etching-induced surface contamination can reduce the exciton quality and thus the light-matter interaction strength significantly. Our fabrication approach reduces interfacial irregularities and enables homogeneous large-area polariton lattices for a wide range of applications, such as polarization-control or topological polaritonics.

## I. INTRODUCTION

Exciton-polaritons enable a variety of phenomena, such as polariton lasing [1, 2], topological polaritons [3–5] and bosonic condensation [6–8]. Polaritons are quasiparticles that emerge when a matter excitation couples strongly to light inside a cavity. Among the variety of cavity systems employed for polaritonics, plasmonic surface lattice resonances (SLRs) have emerged as a versatile platform. These resonances appear when the localized surface plasmon resonance (LSPR) of a metal nanoparticle couples to the diffractive orders of the lattice, resulting in a collective excitation. Plasmonic SLRs combine the strong field confinement of LSPRs with high quality (Q) factors and have been used to realize photoluminescence (PL) enhancement [9], lasing [10], and polaritons [11, 12]. Owing to their large oscillator strengths and exciton binding energies, excitons in monolayer transition metal dichalcogenides (TMDs) are an ideal matter constituent for polaritons with demonstrations ranging from cryogenic [13–15] to room temperature [12, 16, 17].

Due to their inherently two-dimensional (2D) character, excitons in TMDs exhibit a strong sensitivity to their environment, including strain [18] and dielectric disorder [19].

Encapsulation of TMDs in high-quality hBN to form van der Waals heterostructures has become indispensable for samples with good optical quality, with the hBN serving as a clean and flat dielectric environment [20]. To couple emitters to a nanophotonic structure, such as plasmonic nanoparticles, a metasurface or a photonic crystal, the 2D material is commonly either placed on top of the nanostructure [12, 21–23] or the structure is patterned directly on top of the material [11, 24, 25]. Additionally, recent advances were made in transferring nanostructures on top of an hBN carrier-layer onto an active medium [26]. However, in these schemes it is difficult to bring the emitter close to the near-field of the resonator without inducing strain and while ensuring encapsulation in hBN, since even a thin layer of hBN between emitter and resonator has a detrimental impact on the coupling strength. Recently, we reported on a novel fabrication method that addresses this issue by fully integrating a plasmonic cavity into an encapsulating hBN layer and thus into a van der Waals heterostructure providing direct proximity to the near-field without inducing strain [27].

\* alexander.hoegle@lmu.de

† f.tabataba@tu-braunschweig.de

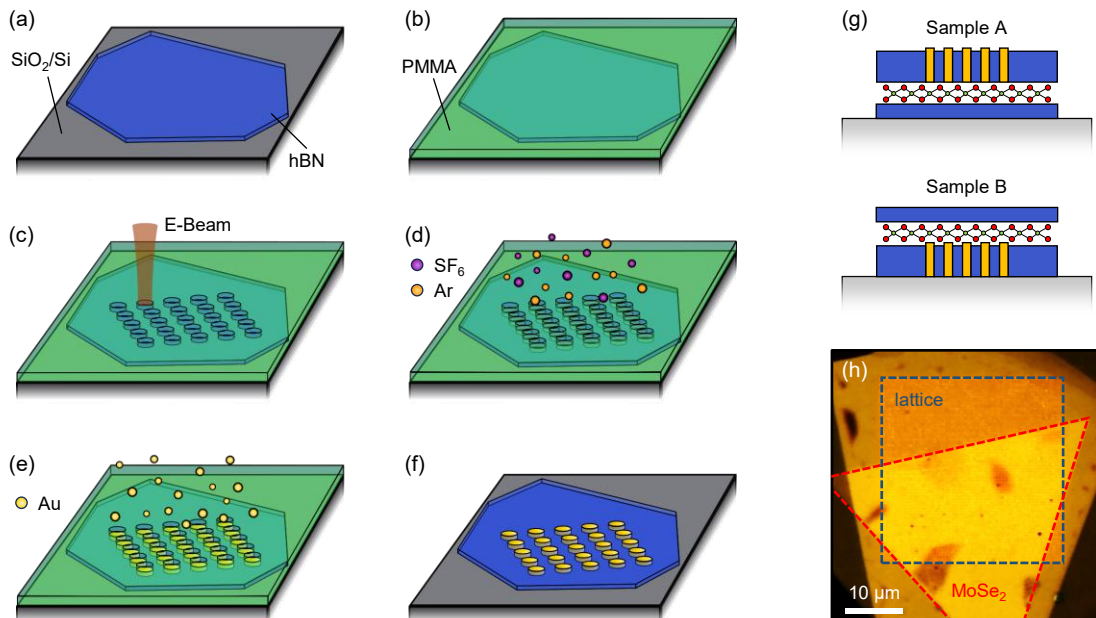


FIG. 1. **Fabrication of gold nanodisk arrays embedded in hBN.** Fabrication sequence: (a) mechanical exfoliation of an hBN flake on a  $\text{SiO}_2/\text{Si}$  substrate, (b) hBN flake covered with a PMMA film, (c) electron-beam lithography, (d) ICP-RIE process of the lattice, (e) gold deposition and (f) removal of the PMMA film. (g) Schematics of the two sample geometries. (h) Optical micrograph of sample A.

Here, we employ two fabrication schemes based on the method developed in Ref. [27], comparing the influence of opposite layer order and using large-area  $\text{MoSe}_2$  monolayers synthesized by chemical vapor deposition (CVD). In sample A, the hBN/plasmonic lattice was placed at the top of the heterostack, while it is at the bottom in sample B. We investigated exciton quality and homogeneity at cryogenic temperatures by differential reflectance (DR) and PL spectroscopy and found narrower linewidths and larger homogeneity of the exciton energy in sample A than in sample B. Using momentum-space DR and PL spectroscopy we further investigated the exciton-photon coupling and determined 25% larger coupling strengths for polaritons in sample A than in sample B due to preserved oscillator strength and a strain-free environment of the exciton.

## II. RESULTS AND DISCUSSION

Plasmonic gold nanodisk arrays embedded in hBN were fabricated by employing electron-beam lithography (EBL) and inductively-coupled plasma reactive ion etching (ICP-RIE) in a stepwise fabrication process displayed in Figs. 1(a)-(f). HBN flakes were prepared via mechanical exfoliation from bulk crystals [Fig. 1(a)] and a square nanodisk array was defined via EBL using PMMA 950 K resist at an average dose of  $500 \mu\text{C}/\text{cm}^2$  [Figs. 1(b) and (c)]. Holes were etched through the hBN layers via

ICP-RIE at an ICP power of 70 W and RF power of 6 W using 5 sccm of Ar and 10 sccm of  $\text{SF}_6$  at a constant chamber pressure of 10 mTorr resulting in an etch rate of  $0.6 \text{ nm/s}$  [Fig. 1(d)]. After etching, a gold film matching the thickness of the hBN layer was deposited via electron-beam evaporation in ultra-high vacuum [Fig. 1(e)]. The lift-off was performed in acetone and isopropanol and the remaining residues were removed with an  $\text{O}_2$  plasma [Fig. 1(f)]. The resulting top surface of the gold disks showed an irregular shape mimicking the etch profile, but the backside exhibited a flat and smooth surface [27].

We fabricated two samples with opposite layer orders. Both samples consist of an hBN-embedded plasmonic lattice, a  $\text{MoSe}_2$  monolayer and a second hBN encapsulation layer. In sample A, the hBN/lattice was placed on top of the stack, while it is the bottom layer in sample B, as shown in Fig. 1(g). Fig. 1(h) shows an optical micrograph of the final stack of sample A exhibiting only a small amount of lattice irregularities. In sample B, the elevated gold disks induce strain in the monolayer, whereas the bottom side of the disks provide a flat interface in sample A. Additionally, the top surface of the processed hBN layer was exposed to  $\text{O}_2$  plasma, which induces defects [28] and modifies the surface composition [29]. The bottom surface of the hBN/lattice, on the other hand, was not exposed to any plasma treatment, and thus should provide a clean and flat interface for the  $\text{MoSe}_2$  monolayer in sample A [27].

We begin our comparison of the two sample schemes

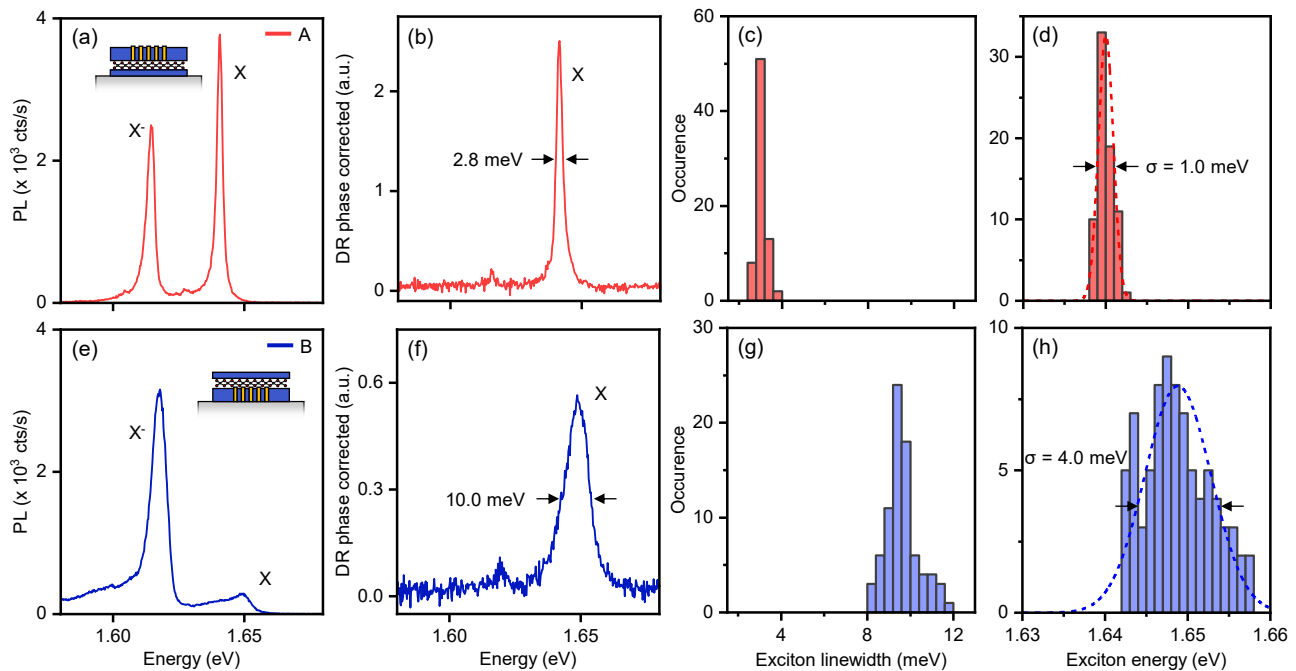


FIG. 2. **Monolayer characteristics.** (a) Representative PL and (b) Kramers-Kronig phase-corrected DR spectra of sample A with the linewidth indicated by black arrows. In inset in (a) indicates the sample geometry. (c) Distribution of the exciton linewidth and (d) resonance energy in an isolated MoSe<sub>2</sub> region on sample A with dashed lines indicating a Gaussian distribution of the resonance energy and arrows marking the standard deviation. (e)-(h) Same as (a)-(d) but for sample B.

by investigating the matter constituents via confocal DR and PL spectroscopy at  $T = 4$  K in hBN-encapsulated monolayer regions in the two samples. Sample A displays emission from both neutral exciton and trion [see Fig. 2(a)], with linewidths down to 2.4 meV, close to the intrinsic limit of around 1 meV [30], a clear sign of a pristine dielectric environment in spite of the additional fabrication steps. Sample B, on the other hand, exhibits a largely suppressed emission from the neutral exciton [Fig. 2(e)] and is dominated by a strong trion emission, a sign of charge doping induced from O<sub>2</sub> plasma cleaning [31, 32]. Additionally, both emission lines exhibit asymmetries with broadened linewidths. Similarly to PL, sample A shows narrow absorption of the neutral exciton, whereas sample B shows a broadened absorption resonance with  $\sim 25\%$  lower oscillator strength as determined by integrating over the peaks in the phase-corrected DR spectra of samples A and B in Figs. 2(b) and (f), respectively.

For a quantitative study, we analyzed the absorption of the neutral exciton over an area of  $\sim 20 \mu\text{m}^2$  for both samples that we raster-scanned with a diffraction-limited optical spot. Figs. 2(c) and (g) show the corresponding distributions of the exciton linewidths for samples A and B, respectively. Sample A displays an average narrow linewidth of 3.0 meV compared to the much broader linewidth of 9.6 meV in sample B. Similarly, the exciton energy is homogeneous with a standard deviation  $\sigma_X \approx 1.0$  meV around  $E_X \approx 1.64$  eV in sample A [Fig. 2(d)]

compared to  $\sigma_X \approx 4.0$  meV around  $E_X \approx 1.649$  eV in sample B [Fig. 2(h)]. The narrow linewidths and spatial homogeneity emphasize the clean and homogeneous dielectric environment in sample A, while the data of sample B suggest increased interfacial contamination.

For the investigation of light-matter coupling, we studied the momentum-resolved dispersions of the coupled exciton-plasmon systems, as shown in Figs. 3 (a) and (e) for the degenerate, hyperbolic lattice dispersions of samples A and B, respectively. The SLRs are well-described by a simple geometric model of the diffractive orders of the lattice [33] (see Ref. [27] for a detailed discussion of this structure). We find that the layer order does not critically impact the linewidth of the SLR and extract linewidths and Q factors of 52.1 meV and 32 for sample A, and 41.9 meV and 40 for sample B.

In both samples, we observe avoided crossings as the cavity energy approaches the exciton energy, which is a hallmark of strong coupling and evidences the formation of exciton-polaritons, in addition to an uncoupled exciton fraction, as seen in Figs. 3(a) and (e). This uncoupled exciton population is likely situated in areas between the gold disks and away from their respective maximum near-fields [34].

We employed a coupled oscillator model [35] to compare the exciton-photon coupling strengths in the two

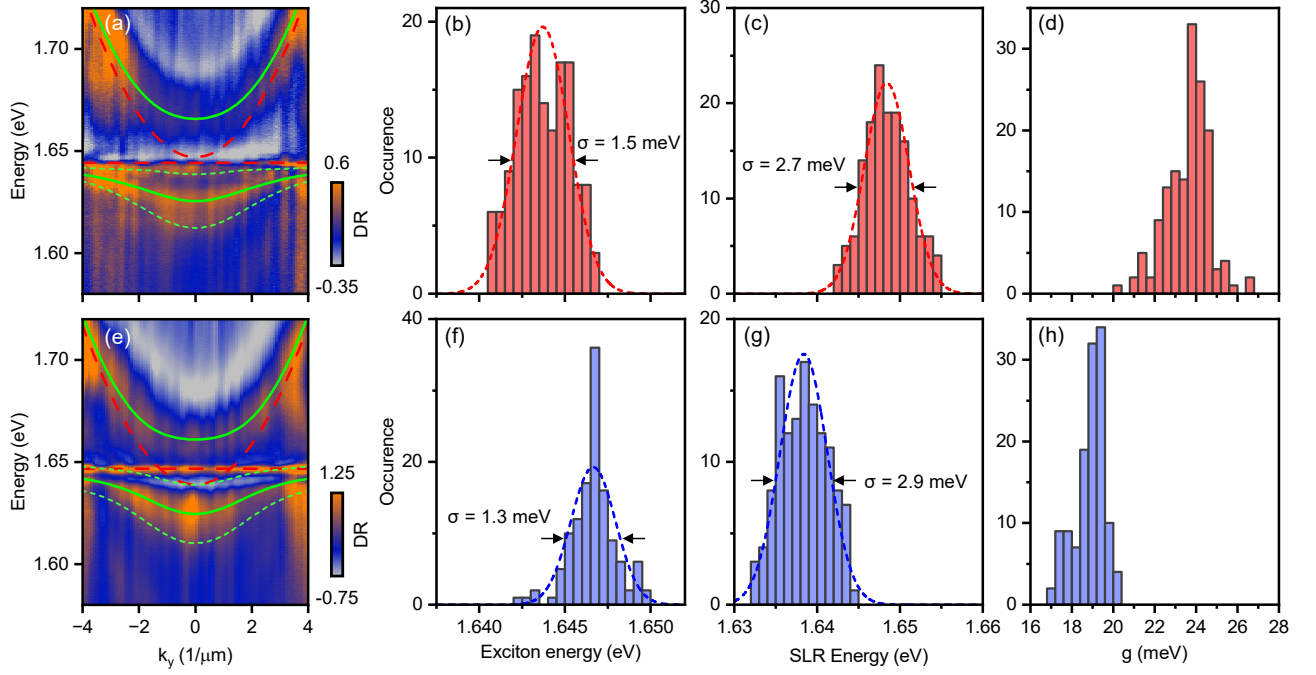


FIG. 3. **Exciton-plasmon coupling characteristics.** (a) Representative momentum-resolved polariton dispersion of sample A in DR with solid lines highlighting the fitted polariton branches and dashed lines indicating the exciton and SLR resonance energies. (b) Distribution of the resonance energy of the AIs exciton and (c) the SLR at  $k = 0$  in sample A with dashed lines indicating a Gaussian distribution and the standard deviation marked by arrows. (d) Distribution of the exciton-plasmon coupling strength in sample A. (e)-(h) Same as (a)-(d) but for sample B.

samples. The Hamiltonian reads

$$H = \begin{pmatrix} E_X - i\gamma_X & g \\ g & E_{SLR} - i\gamma_{SLR} \end{pmatrix}, \quad (1)$$

where  $E_X$  ( $E_{SLR}$ ) and  $\gamma_X$  ( $\gamma_{SLR}$ ) are the exciton (SLR) energy and half-width at half-maximum and  $g$  denotes the light-matter coupling strength. The energy eigenvalues for the upper ( $E_{UP}$ ) and lower polariton ( $E_{LP}$ ) branches obtained by diagonalizing  $H$  are

$$E_{UP,LP} = \frac{E_{SLR} + E_X - i(\gamma_X - \gamma_{SLR})}{2} \pm \sqrt{g^2 - \frac{1}{4}[E_X - E_{SLR} - i(\gamma_X - \gamma_{SLR})]^2}. \quad (2)$$

We fitted the dispersions in Figs. 3(a) and (e) by tracking the DR maxima and found a higher coupling strength in sample A ( $g = 23.5$  meV) as opposed to sample B ( $g = 19.5$  meV), which we assign to the aforementioned difference in exciton oscillator strength [see Figs. 2(b) and (f)]. The Rabi splitting, defined as  $\Omega = \sqrt{4g^2 - (\gamma_X - \gamma_{SLR})^2}$ , is 40.1 and 35.5 meV for samples A and B, respectively. In addition to the dispersions of the upper and lower polariton branches, we plot the linewidth of the lower polariton branch  $\gamma_{LP}$  [see Fig. 3(a) and (e)]. The linewidth is obtained from

$$\gamma_{LP} = |X|^2\gamma_X + |C|^2\gamma_{SLR} \quad (3)$$

with the Hopfield coefficients [36] given by

$$|X|^2 = \frac{1}{2} \left[ 1 + \frac{E_{SLR} - E_X}{\sqrt{\Omega^2 + (E_{SLR} - E_X)^2}} \right] \quad (4)$$

$$|C|^2 = \frac{1}{2} \left[ 1 - \frac{E_{SLR} - E_X}{\sqrt{\Omega^2 + (E_{SLR} - E_X)^2}} \right]. \quad (5)$$

We determined the exciton and SLR resonance energies, as well as the coupling strength across large areas of the two samples by fitting the coupled oscillator model to the data of every spatial position in 2D raster-scan momentum-space DR spectroscopy. The distribution of the exciton resonance energy at  $k = 0$  of sample A in Fig. 3(b) shows a standard deviation  $\sigma = 1.5$  meV, comparable to the bare exciton region, highlighting the preserved clean environment for the exciton in spite of the presence of the lattice. Sample B displays a similar homogeneity with  $\sigma = 1.3$  meV in the hybrid region [see Fig. 3(f)]. The SLR resonance energies in sample A and B, shown in Figs. 3(c) and (g) respectively, exhibit comparable standard deviations for both samples. Hence, the layer order in the sample does not impact the homogeneity of the SLR resonance significantly, similar to the linewidth. Figs. 3(d) and (h) display the distributions of the obtained coupling strengths  $g$  for samples A and B, respectively. We obtain average  $g$  values and standard deviations of  $23.6 \pm 1$  and  $18.9 \pm 0.7$  meV, as well

as maximum  $g$  values of 26.4 and 20.2 meV for samples A and B, respectively, demonstrating elevated coupling strengths in sample A over large areas. This is consistent with the results obtained for the bare exciton with larger oscillator strength in this sample.

### III. CONCLUSION

In summary, we studied exciton-polaritons in samples with plasmonic SLRs coupled to MoSe<sub>2</sub> monolayers. Using a fabrication method that allows to embed plasmonic lattices into thin hBN layers and thus integrate them into van der Waals heterostructures [27], we compared two samples with opposite layer order. We found that placing the hBN-embedded plasmonic lattice on top of the stack yielded high quality, narrow excitonic absorption and PL, while fabrication-induced surface irregularities and doping resulted in broader exciton resonances with reduced oscillator strength when the lattice was placed at the bottom of the stack. Momentum-resolved DR dispersions at 4 K exhibited avoided crossings, demonstrating strong exciton-photon coupling in both geometries. Fitting a coupled oscillator model across large areas revealed a 25% increased coupling strength for the sample, in which the hBN-embedded plasmonic lattice was placed on top of the TMD monolayer, resulting in a clean and strain-free dielectric environment and preserved oscillator strength. Beyond the comparison of layer order presented here, our fabrication method establishes a versatile platform for exploring integration of sensitive van der Waals materials into nanophotonic device architectures with potential applications in polariton circuitry and topological photonics [4, 37, 38].

### IV. METHODS

#### A. Synthesis of MoSe<sub>2</sub> monolayers

We synthesized large-area high-quality MoSe<sub>2</sub> monolayers using a CVD system (Carbolite Gero) with a three-zone furnace and a 1-inch quartz tube. The vapor phase chalcogenization method was used with MoO<sub>2</sub> and Se powders (99.99%, Sigma-Aldrich) as precursors [39]. The target substrates, Si chips with 285 nm SiO<sub>2</sub>, were suspended face-down over an aluminum crucible with MoO<sub>2</sub> powder placed at the center of the first heating zone. 10 cm upstream from the center, another crucible with Se powder was placed. The tube was evacuated to 10 mTorr several times to remove air and moisture and 300 sccm of ultra-high purity Ar was flowed into the chamber to act as a carrier gas at ambient pressure in an inert atmosphere. For the growth, the furnace temperature was increased at a rate of 10°C/min to 750°C and maintained for 15 min. When the temperature reached 750°C, 0.75 sccm of H<sub>2</sub> was introduced as a reductant gas. After the growth, the furnace was cooled down to room temperature.

#### B. Sample design and assembly

We employed the finite-difference time-domain method (software Lumerical) to design the gold nanodisk arrays. We simulated gold nanodisks with diameter of 70 nm organized on a square lattice with a lattice constant of 500 nm. The heights of the disks were designed between 30 and 50 nm matching the thickness of the hBN layer, in which they were incorporated. We then selected the thickness of the second hBN layer such that the simulated resonance energy matched the energy of the neutral 1s exciton in the MoSe<sub>2</sub> monolayer.

For the sample assembly, we used a polymer assisted dry stamping method based on poly-bisphenol A-carbonate (PC, Sigma Aldrich) and polycaprolacton (PCL, Sigma Aldrich). For the pick-up of the lattices, PCL stamps yielded a higher success rate and reproducibility compared to PC. The transfer with PCL was performed by heating to 57°C after contact, below the melting point (60°C) [40], followed by a pick-up at 30°C. For sample B, we released the hBN/lattice flake onto the target substrate at 75°C and cleaned it in THF, acetone, and isopropanol. The top hBN and CVD-grown MoSe<sub>2</sub> flakes were picked up successively with a PC stamp at 95°C and the stack was released onto the hBN/lattice flake at 195°C. For sample A, the hBN/lattice flake was released onto a CVD-grown MoSe<sub>2</sub> monolayer at 75°C and cleaned in THF, acetone, and isopropanol. Then a PC stamp was used to pick up the stack at 95°C, followed by release onto a pre-transferred (with PC) bottom hBN flake at 195°C. PC was removed in chloroform, acetone, and isopropanol. Both samples were annealed in ultra-high vacuum at 200°C for 15 h to remove residues and trapped air from the interfaces.

#### C. Optical spectroscopy

We performed cryogenic DR and PL spectroscopy in backscattering geometry in a closed-cycle cryostat (attocube systems, attoDRY800) operating at a temperature of 4 K. Piezo-units (attocube systems, ANPx101, ANPz101, and ANSxy100) were used to position the sample with respect to a low temperature apochromatic objective (LT-APO/633-RAMAN/0.81). A lab-built Fourier imaging setup in 4f and telescope configuration employing four achromatic doublet lenses (Edmund Optics, VIS-NIR with focal lengths of 750, 750, 400 and 150 mm) was used to measure angle-resolved DR and PL spectra. A spectrometer (Teledyne Princeton Instruments, IsoPlane SCT320) with a 300 grooves/mm grating was used to disperse the signal, which was detected by a Peltier-cooled charge-coupled device (CCD) (Teledyne Princeton Instruments, PIXIS 1024). We converted camera pixel to wavevector in  $1/\mu\text{m}$  using the relation  $k_{\parallel} = \sin(\Theta)k_0$  with the maximum angle  $\Theta$  given by the numerical aperture of the objective, the illuminated area on the CCD, and the light wavevector  $k_0 = 2\pi/\lambda$ .

For DR, we used a pulsed supercontinuum laser (NKT Photonics, SuperK with Varia filter). DR was calculated using the reflectance  $R$  from the lattice or hybrid region and the background  $R_0$  from a region containing only hBN and was defined as  $DR = (R - R_0)/R_0$ . Exciton resonance linewidths and oscillator strengths were extracted using Kramers-Kronig relation and Lorentzian fits. PL was excited with an external cavity diode laser (New Focus, Velocity) emitting at 635 nm with excitation powers ranging from 7  $\mu$ W to 30  $\mu$ W.

**Acknowledgements:** This research was funded by the European Research Council (ERC) under the Grant Agreement No. 772195 and the Deutsche Forschungsgemeinschaft (DFG, German Research Foundation) within Germany's Excellence Strategy under grant No. EXC-2111-390814868. K.W. and T.T. acknowledge support from the CREST (JPMJCR24A5), JST and World Premier International Research Center Initiative (WPI), MEXT, Japan. I.B. acknowledges funding from the Alexander von Humboldt Foundation. F.T.-V. acknowledges funding from the Munich Center for Quantum Science and Technology (MCQST) and the European Union's Framework Programme for Research and Innovation Horizon Europe under the Marie Skłodowska-Curie Actions grant agreement No. 101058981.

## REFERENCES

- [1] C. Schneider, A. Rahimi-Iman, N. Y. Kim, J. Fischer, I. G. Savenko, M. Amthor, M. Lermer, A. Wolf, L. Worschech, V. D. Kulakovskii, I. A. Shelykh, M. Kamp, S. Reitzenstein, A. Forchel, Y. Yamamoto, and S. Höfling, An electrically pumped polariton laser, *Nature* **497**, 348 (2013).
- [2] T. H. Harder, M. Sun, O. A. Egorov, I. Vakulchyk, J. Beierlein, P. Gagel, M. Emmerling, C. Schneider, U. Peschel, I. G. Savenko, S. Klemmt, and S. Höfling, Coherent topological polariton laser, *ACS Photon.* **8**, 1377 (2021).
- [3] S. Klemmt, T. Harder, O. Egorov, K. Winkler, R. Ge, M. Bandres, M. Emmerling, L. Worschech, T. Liew, M. Segev, C. Schneider, and S. Höfling, Exciton-polariton topological insulator, *Nature* **562**, 552 (2018).
- [4] W. Liu, Z. Ji, Y. Wang, G. Modi, M. Hwang, B. Zheng, V. J. Sorger, A. Pan, and R. Agarwal, Generation of helical topological exciton-polaritons, *Science* **370**, 600 (2020).
- [5] M. Li, I. Sinev, F. Benimetskiy, T. Ivanova, E. Khestanova, S. Kiriushechkina, A. Vakulenko, S. Guddala, M. Skolnick, V. M. Menon, D. Krizhanovskii, A. Alù, A. Samusev, and A. B. Khanikaev, Experimental observation of topological  $Z_2$  exciton-polaritons in transition metal dichalcogenide monolayers, *Nat. Commun.* **12**, 4425 (2021).
- [6] J. Kasprzak, M. Richard, S. Kundermann, A. Baas, P. Jeambrun, J. M. J. Keeling, F. Marchetti, M. Szymańska, R. André, J. Staehli, V. Savona, P. Littlewood, B. Deveaud, and L. S. Dang, Bose-Einstein condensation of exciton polaritons, *Nature* **443**, 409 (2006).
- [7] C. Anton-Solanas, M. Waldherr, M. Klaas, H. Suchomel, T. H. Harder, H. Cai, E. Sedov, S. Klemmt, A. V. Kavokin, S. Tongay, K. Watanabe, T. Taniguchi, S. Höfling, and C. Schneider, Bosonic condensation of exciton-polaritons in an atomically thin crystal, *Nat. Mater.* **20**, 1233 (2021).
- [8] J. Zhao, R. Su, A. Fieramosca, W. Zhao, W. Du, X. Liu, C. Diederichs, D. Sanvitto, T. C. Liew, and Q. Xiong, Ultralow threshold polariton condensate in a monolayer semiconductor microcavity at room temperature, *Nano Lett.* **21**, 3331 (2021).
- [9] B. Lee, J. Park, G. H. Han, H.-S. Ee, C. H. Naylor, W. Liu, A. C. Johnson, and R. Agarwal, Fano resonance and spectrally modified photoluminescence enhancement in monolayer MoS<sub>2</sub> integrated with plasmonic nanoantenna array, *Nano Lett.* **15**, 3646 (2015).
- [10] W. Zhou, M. Dridi, J. Y. Suh, C. H. Kim, D. T. Co, M. R. Wasielewski, G. C. Schatz, and T. W. Odom, Lasing action in strongly coupled plasmonic nanocavity arrays, *Nat. Nanotechnol.* **8**, 506 (2013).
- [11] W. Liu, B. Lee, C. H. Naylor, H.-S. Ee, J. Park, A. C. Johnson, and R. Agarwal, Strong exciton-plasmon coupling in MoS<sub>2</sub> coupled with plasmonic lattice, *Nano Lett.* **16**, 1262 (2016).
- [12] S. Wang, Q. Le-Van, F. Vaianella, B. Maes, S. Eizagirre Barker, R. H. Godiksen, A. G. Curto, and J. Gomez Rivas, Limits to strong coupling of excitons in multilayer WS<sub>2</sub> with collective plasmonic resonances, *ACS Photon.* **6**, 286 (2019).
- [13] X. Liu, T. Galfsky, Z. Sun, F. Xia, E.-c. Lin, Y.-H. Lee, S. Kéna-Cohen, and V. M. Menon, Strong light-matter coupling in two-dimensional atomic crystals, *Nat. Photon.* **9**, 30 (2015).
- [14] S. Dufferwiel, S. Schwarz, F. Withers, A. Trichet, F. Li, M. Sich, O. Del Pozo-Zamudio, C. Clark, A. Nalitov, D. Solnyshkov, G. Malpuech, K. S. Novoselov, J. M. Smith, M. S. Skolnick, D. N. Krizhanovskii, and A. I. Tartakovskii, Exciton-polaritons in van der Waals heterostructures embedded in tunable microcavities, *Nat. Commun.* **6**, 8579 (2015).
- [15] C. Schneider, M. M. Glazov, T. Korn, S. Höfling, and B. Urbaszek, Two-dimensional semiconductors in the regime of strong light-matter coupling, *Nat. Commun.* **9**, 2695 (2018).
- [16] Z. Sun, J. Gu, A. Ghazaryan, Z. Shotan, C. R. Consideine, M. Dollar, B. Chakraborty, X. Liu, P. Ghaemi, S. Kéna-Cohen, and V. M. Menon, Optical control of room-temperature valley polaritons, *Nat. Photon.* **11**, 491 (2017).
- [17] L. Zhang, R. Gogna, W. Burg, E. Tutuc, and H. Deng, Photonic-crystal exciton-polaritons in monolayer semiconductors, *Nat. Commun.* **9**, 713 (2018).
- [18] Z. Khatibi, M. Feierabend, M. Selig, S. Brem, C. Linderälvi, P. Erhart, and E. Malic, Impact of strain on the excitonic linewidth in transition metal dichalcogenides, *2D Mater.* **6**, 015015 (2018).
- [19] A. Raja, L. Waldecker, J. Zipfel, Y. Cho, S. Brem, J. D. Ziegler, M. Kulig, T. Taniguchi, K. Watanabe, E. Malic, T. F. Heinz, T. C. Berkelbach, and A. Chernikov, Dielectric disorder in two-dimensional materials, *Nat. Nanotechnol.* **14**, 832 (2019).
- [20] F. Cadiz, E. Courtade, C. Robert, G. Wang, Y. Shen, H. Cai, T. Taniguchi, K. Watanabe, H. Carrere, D. Lagarde, M. Manca, T. Amand, P. Renucci, S. Tongay,

- X. Marie, and B. Urbaszek, Excitonic linewidth approaching the homogeneous limit in MoS<sub>2</sub>-based van der Waals heterostructures, *Phys. Rev. X* **7**, 021026 (2017).
- [21] L. Sortino, P. Zotev, S. Mignuzzi, J. Cambiasso, D. Schmidt, A. Genco, M. Aßmann, M. Bayer, S. Maier, R. Sapienza, and A. I. Tartakovskii, Enhanced light-matter interaction in an atomically thin semiconductor coupled with dielectric nano-antennas, *Nat. Commun.* **10**, 5119 (2019).
- [22] S. Vadia, J. Scherzer, K. Watanabe, T. Taniguchi, and A. Högele, Magneto-optical chirality in a coherently coupled exciton–plasmon system, *Nano Lett.* **23**, 614 (2023).
- [23] A. J. Moilanen, M. Cavigelli, T. Taniguchi, K. Watanabe, and L. Novotny, Electrical control of photoluminescence in 2D semiconductors coupled to plasmonic lattices, *ACS Nano* **19**, 4731 (2025).
- [24] W. Liu, Y. Wang, B. Zheng, M. Hwang, Z. Ji, G. Liu, Z. Li, V. J. Sorger, A. Pan, and R. Agarwal, Observation and active control of a collective polariton mode and polaritonic band gap in few-layer WS<sub>2</sub> strongly coupled with plasmonic lattices, *Nano Lett.* **20**, 790 (2019).
- [25] J. Sun, Y. Li, H. Hu, W. Chen, D. Zheng, S. Zhang, and H. Xu, Strong plasmon–exciton coupling in transition metal dichalcogenides and plasmonic nanostructures, *Nanoscale* **13**, 4408 (2021).
- [26] F. Dorey, J. D. Ziegler, A. J. Moilanen, O. Hordiiichuk, G. Nagamine, T. Taniguchi, K. Watanabe, D. J. Norris, M. V. Kovalenko, G. Raino, and L. Novotny, Transferable plasmonic arrays enabling strong coupling with layered perovskites in an active diode architecture, *Nano Lett.* **26**, 1616 (2025).
- [27] F. Tabataba-Vakili, L. Krelle, L. Husel, H. P. Nguyen, Z. Li, I. Bilgin, K. Watanabe, T. Taniguchi, and A. Högele, Metasurface of strongly coupled excitons and nanoplasmonic arrays, *Nano Lett.* **24**, 10090 (2024).
- [28] J. Comtet, E. Glushkov, V. Navikas, J. Feng, V. Babenko, S. Hofmann, K. Watanabe, T. Taniguchi, and A. Radenovic, Wide-field spectral super-resolution mapping of optically active defects in hexagonal boron nitride, *Nano Lett.* **19**, 2516 (2019).
- [29] Z. Ma, C. Prawoto, Z. Ahmed, Y. Xiao, L. Zhang, C. Zhou, and M. Chan, Control of hexagonal boron nitride dielectric thickness by single layer etching, *J. Mater. Chem. C* **7**, 6273 (2019).
- [30] G. Moody, C. Kavir Dass, K. Hao, C.-H. Chen, L.-J. Li, A. Singh, K. Tran, G. Clark, X. Xu, G. Berghäuser, E. Malic, A. Knorr, and X. Li, Intrinsic homogeneous linewidth and broadening mechanisms of excitons in monolayer transition metal dichalcogenides, *Nat. Commun.* **6**, 8315 (2015).
- [31] S. Kim, M. S. Choi, D. Qu, C. H. Ra, X. Liu, M. Kim, Y. J. Song, and W. J. Yoo, Effects of plasma treatment on surface properties of ultrathin layered MoS<sub>2</sub>, *2D Mater.* **3**, 035002 (2016).
- [32] S. Wu, Y. Zeng, X. Zeng, S. Wang, Y. Hu, W. Wang, S. Yin, G. Zhou, W. Jin, T. Ren, *et al.*, High-performance p-type MoS<sub>2</sub> field-effect transistor by toroidal-magnetic-field controlled oxygen plasma doping, *2D Mater.* **6**, 025007 (2019).
- [33] R. Guo, T. K. Hakala, and P. Törmä, Geometry dependence of surface lattice resonances in plasmonic nanoparticle arrays, *Phys. Rev. B* **95**, 155423 (2017).
- [34] L. Greten, R. Salzwedel, T. Göde, D. Greten, S. Reich, S. Hughes, M. Selig, and A. Knorr, Strong coupling of two-dimensional excitons and plasmonic photonic crystals: microscopic theory reveals triplet spectra, *ACS Photon.* **11**, 1396 (2024).
- [35] V. Savona, L. Andreani, P. Schwendimann, and A. Quattropani, Quantum well excitons in semiconductor microcavities: Unified treatment of weak and strong coupling regimes, *Solid State Commun.* **93**, 733 (1995).
- [36] J. Hopfield, Theory of the contribution of excitons to the complex dielectric constant of crystals, *Phys. Rev.* , 1555 (1958).
- [37] L. Wang, R.-Y. Zhang, M. Xiao, D. Han, C. T. Chan, and W. Wen, The existence of topological edge states in honeycomb plasmonic lattices, *N. J. Phys.* **18**, 103029 (2016).
- [38] M. Honari-Latifpour and L. Yousefi, Topological plasmonic edge states in a planar array of metallic nanoparticles, *Nanophotonics* **8**, 799 (2019).
- [39] I. Bilgin, A. S. Raeliarijaona, M. C. Lucking, S. C. Hodge, A. D. Mohite, A. de Luna Bugallo, H. Terrones, and S. Kar, Resonant raman and exciton coupling in high-quality single crystals of atomically thin molybdenum diselenide grown by vapor-phase chalcogenization, *ACS Nano* **12**, 740 (2018).
- [40] S. Son, Y. J. Shin, K. Zhang, J. Shin, S. Lee, H. Idzuchi, M. J. Coak, H. Kim, J. Kim, J. H. Kim, M. Kim, D. Kim, P. Kim, and J.-G. Park, Strongly adhesive dry transfer technique for van der Waals heterostructure, *2D Mater.* **7**, 041005 (2020).